J Solid State Electrochem (2012) 16:3045–3058
DOI 10.1007/s10008-012-1735-2

ORIGINAL PAPER

Proposed model for quantification of dissolution—and evolution of a steel-CO_2 solution interface by the transmission line approach

H. Castaneda · M. Galicia

Received: 1 December 2011 / Revised: 17 March 2012 / Accepted: 19 March 2012 / Published online: 22 April 2012

Abstract The corrosion mechanisms occurring at the homogeneous porous layer was determined assuming that the pores had a cylindrical geometry, and that the initial interface of a carbon steel-CO_2 solution behaved as a transmission line (TL). TL modeling quantitatively assessed the impedance distribution and the mesoporous layer formation and evolution at the interface, while describing the physical characteristics of the mesoporous $FeCO_3$ layer at the base and wall within the initial pore. The TL helped to characterize four stages during the interfacial evolution: active, active-porous layer, mixed layer, and the reactive stages. Using TLs helped to quantify the dissolution process and distinguish the mechanisms with good agreement between calculated magnitudes and experimental data.

Keywords CO_2 corrosion · TLM · Steel interface · EIS · Steel dissolution

Introduction

Experimental testing on carbon steel exposed to CO_2 aqueous environments has shown different forms of localized corrosion. The cause of localized corrosion includes mesoscale attack, influence of the interface, and processes related to the type of material or electrolyte conditions [1]. CO_2 corrosion depends on key factors, such as temperature, CO_2 partial pressure, pH, metallic microstructure [2–4] and corrosion products [5]. Research in CO_2-saturated environments has determined that long immersion times result in a dissolution rate that will be lowered and stabilized by the precipitation of a passive layer of $FeCO_3$ [5–7]. According to Nesic et al., $FeCO_3$ is the most stable layer which precipitates above 50°C if the pH of the solution is from 6 to 7 and if the solubility limit of Fe^{2+} and CO_3^{2-} ions reaches precipitation magnitudes [8]. Farelas et al. reported a $FeCO_3$ layer that formed as a consequence of the selective dissolution of the ferrite phase (α-Fe) [9] in mild steel. Thereafter, the presence of the Fe_3C phase produces a microgalvanic effect at the surface. They monitored and characterized the interface by using equivalent electrical analogs. Also, the results revealed the evolution process, which can be described by three different stages. These stages are named: (1) active-adsorption state, (2) active-porous layer state, and (3) mixed-porous layer state. The stages represent the surface mechanism and qualitative corrosion product layer properties, such as the porosity.

The porous nature of the corrosion products has influenced the corrosion dissolution at different electrochemical/corrosion interfaces [9, 10]. The morphology and physical distribution have also influenced the mechanisms occurring at the interface [11]. Pore geometries, such as cylinders and cones, have resulted in homogeneous mechanisms [12] within the porous layers and at the interface [13] in batteries and different applications of aqueous corrosion [14].

Transmission line (TL) modeling has been used for frequency domain analysis of the formation of different porous layers with different geometries [15–20]. Recently, TL based on impedance data analysis has been successfully used for different aqueous-film interfaces and the solid state

H. Castaneda (✉)
Chemical and Biomolecular Engineering Department,
National Center for Research and Education in Corrosion and Materials Reliability, The University of Akron,
Akron, OH 44325, USA
e-mail: homeroc@uakron.edu

M. Galicia
Departamento de Quimico-Biologicas, ICB,
Universidad Autonoma de Ciudad Juarez,
Ciudad Juarez, Chihuahua 32310, Mexico

[15–18] by assuming different pore geometries and homogeneous–heterogeneous distribution.

The original work from De Levie [21] assumed that the impedance distribution within pores was as a consequence of the effects that resulted from the pore shape such as (a) distributed capacitance, (b) internal ohmic resistance through the porous structures in terms of a "transmission line", and (c) a resulting range of time constants, which in turn, gave rise to the characterization of pore length and diameter [22, 23]. TLs have been applied successfully to impedance distributions in mesoscale and mesoporous surfaces, such as electrochemical supercapacitors [22–25], homogenous geometries for battery electrodes, and heterogeneous layers for corrosion products. The interfacial mechanism and quantification of parameters associated with the layer were deduced by examining the transport properties within the pores [25].

In the present work, we use the impedance distribution of the steel/carbonate/electrolyte interface obtained in our previous work [9]. This distribution was monitored by using an AC electrochemical technique and quantified by applying TLs. The continuous evolution of the initiation, growth and breakdown of the corrosion products formed within the cylindrical porous layer in a flow channel was characterized by assuming mesoporous layer. The inner homogeneous porous layer produced by the metallic dissolution and the outer layer produced by $FeCO_3$ within the pores. Both layers were described in three stages, previously as homogeneous layers [9]. A new stage was added to the evolution process at the interface and is considered in the TL model. The model helps to estimate the dissolution rate and evolution of the steel–CO_2 solution interface and elucidate the mechanisms of reaction at the interface. The intention of the work was to propose an improvement for the quantification of carbon steel at the CO_2 corroding rate while explaining the interfacial mechanisms by using AC methods with TLs.

Material and methods

System setup and experimental conditions

The setup for experiments in the "Thin Channel Flow Cell" or TCFC have been described and illustrated in detail previously [9]. The test section is rectangular with four places for metallic AISI/SAE 1018 steel probes. The experimental electrolyte solution was composed of 3 wt% NaCl, and was recirculated at 126 $m^3\ s^{-1}$ at a fixed temperature of 80°C. The oxygen concentration was maintained at 10 ppb wt.%. The pH of the test solution was adjusted from initial (pH=4.2±0.10) to 6.6± 0.10. The CO_2 partial pressure at 80°C was 5.4×10^4 Pa. Evolution of the interface occurred during 167 h of exposure, and reactive stage 4 commenced after 157 h by the addition of a 1 M H_2SO_4 solution [26] resulting in a electrolyte pH of 5.

Electrochemical cell

The probe used for the electrochemical measurements included a working electrode parallel to the fluid flow, as shown in Fig. 1. This consisted of 1018 carbon steel with a round geometry, having a 0.95 cm^2 surface area besides a concentric 1018 carbon steel ring as reference electrode. An outer 316 stainless steel ring acts a counter-electrode. Details of the surface finish and the chemical composition of the carbon steel was previously described [9].

Electrochemical measurements

Electrochemical impedance spectroscopy (EIS) measurements were taken continuously for 167 h to monitor the flow cell. EIS was measured under a sinusoidal excitation potential of 10 mV (amplitude) in a frequency range from 10 kHz to 10 mHz. The impedance measurements were corroborated by performing a frequency sweep from high to low values, and vice versa, for some data points. KK (Kramers–Kronig) transforms [27] were used for the set of EIS results and corroborate the applicability for the technique.

Results and discussion

The previous work included the porous layer as the initial active state as a result of the selective dissolution of the ferrite phase. The existence of one time constant in the impedance signature in Fig. 2a and b represents the active dissolution. The negative magnitude at short exposure times has been assumed to related adsorption-nonlinear process [9, 28, 29]. The formation of the initial porous layer influences the conditions for the precipitation of corrosion products within the pore. The continuous evolution of the steel/electrolyte interface resulted in two semicircle in the Nyquist complex representation as shown in Fig. 3a, and one maximum in Bode signature at medium frequencies with an indication in low frequencies as displayed in Fig. 3b. The semicircle loops were formed as a consequence of the active-mass transfer processes that existed at the electrode/electrolyte interface. The second stage was characterized by two time constants appearing at 25 h of exposure. The third stage was identified by a passive or stable layer at longer exposure times (>85 h), and the evolution of two loops in the complex and two time constant in Bode representation as shown in Fig. 4a and b, respectively. The evolution of the physical properties of the layer was qualitatively rationalized with equivalent electrical analogs [9].

The addition of sulfuric acid to the electrolyte after 155 h resulted in reactive behavior as a result of a breakdown of the mesoporous corrosion product layer. Modification of the

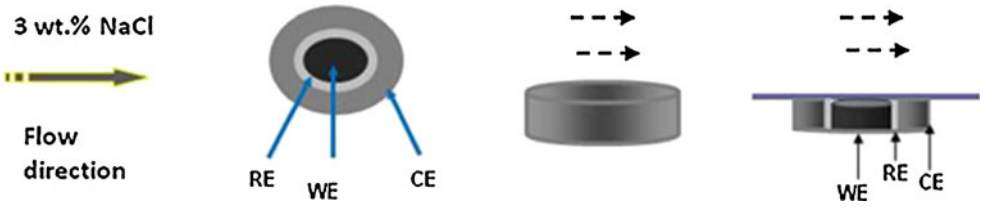

Fig. 1 Scheme of the configuration of the working electrode parallel to the fluid flow

chemical conditions of the electrolyte produced different supersaturation index (SS) magnitudes [6, 28] quantified previously for three stages [9] and currently included in the fourth stage. Figure 5a shows the impedance response following the acid addition, with the second loop that was formed in the previous stage decreasing and disappearing over time. Figure 5b represents the disappearance of the low frequency time constant as a consequence of the interface reactivation. In this work, four stages were characterized and quantified by the TL method, with the addition of the reactivation stage as a result of the acid conditions in the electrolyte.

Transmission line

The interfacial evolution of the steel–CO_2 system, which involved the homogeneous metallic selective dissolution and progressive formation of mesoporous iron carbonate layer at the interface, was the motivation for the use of a more detailed interfacial model. The continuous evolution of the corrosion products within the porous layer at the different interface/location influences the current/impedance distribution. The geometry of the pores accrues the surface interaction with the electrolyte. The pore shape is cylindrical with defined wall and base areas. The selective dissolution as described in a previous work [9] produces initial cylindrical pores during the activation stage after 3 h. Figure 6 illustrates the formation of homogeneous cylindrical pores. The schematic representation shows the surface exposed to the fluid, whereas the orientation

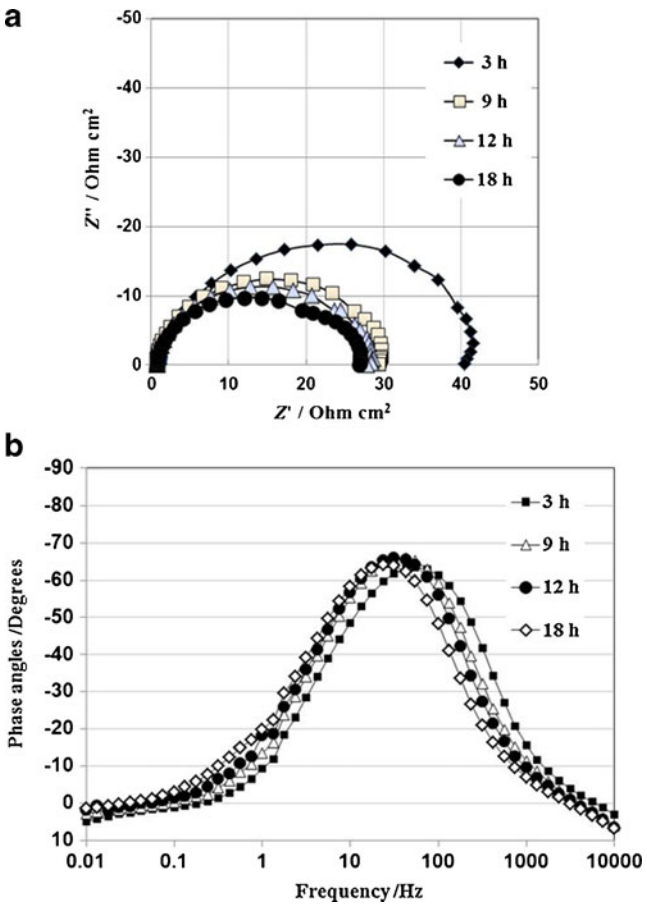

Fig. 2 EIS Nyquist plot (**a**) and phase angle plot (**b**) at different times of exposure to a 3 wt% NaCl solution for stage 1

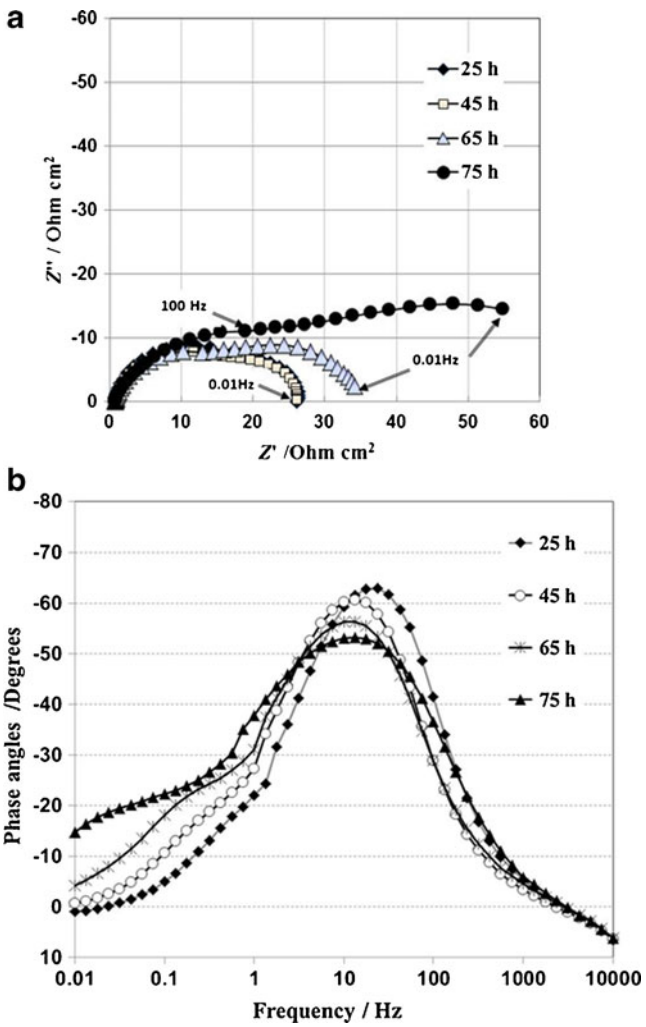

Fig. 3 EIS Nyquist plot (**a**) and phase angle plot (**b**) at different times of exposure to a 3 wt% NaCl solution for stage 2

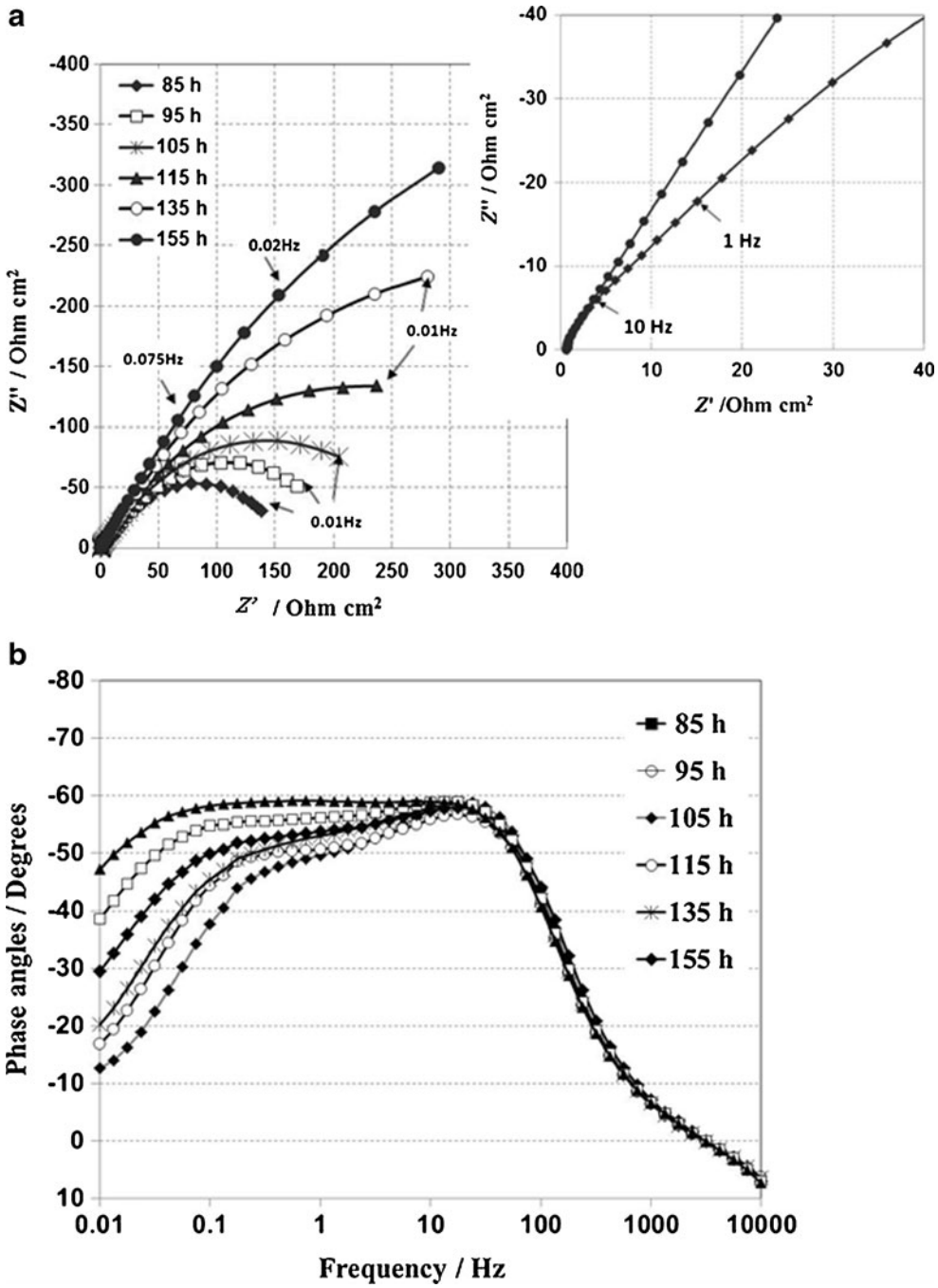

Fig. 4 EIS Nyquist plot (**a**) and phase angle plot (**b**) at different times of exposure to a 3 wt.% NaCl solution for stage 3

for the TL was perpendicular to the fluid motion. The exposed surface represents the total area of the electrode, the metallic structure is subdivided in equal geometries, and each element represents the transport mechanisms occurring at that location.

The evolution from an active to a passive surface includes different mechanisms, with impedance helping to identify the control process with time. A total of three stages have been described, based on the control step process occurring at the interface, and a homogeneously porous layer was assumed to be formed during the stage 1 after 3 h of exposure. The cylinder shape of the pores is used to obtain the characteristics of the boundary conditions and impedance distribution of the surface. De Levie [18, 19, 21] and several other authors [20, 23–25] have made different assumptions for the development of the expressions used for TL in homogeneous porous layers. The main advantage of the finite difference concept is the possibility of introducing mechanisms at each location within the pore interfaces and distinguishing the processes at the boundary conditions, such as the wall and the pore base [17]. In this approach, the pore is separated in the wall and the pore base. Figure 6 indicates the components of the pore, represented by Z_b as the impedance of the base of the pore, and

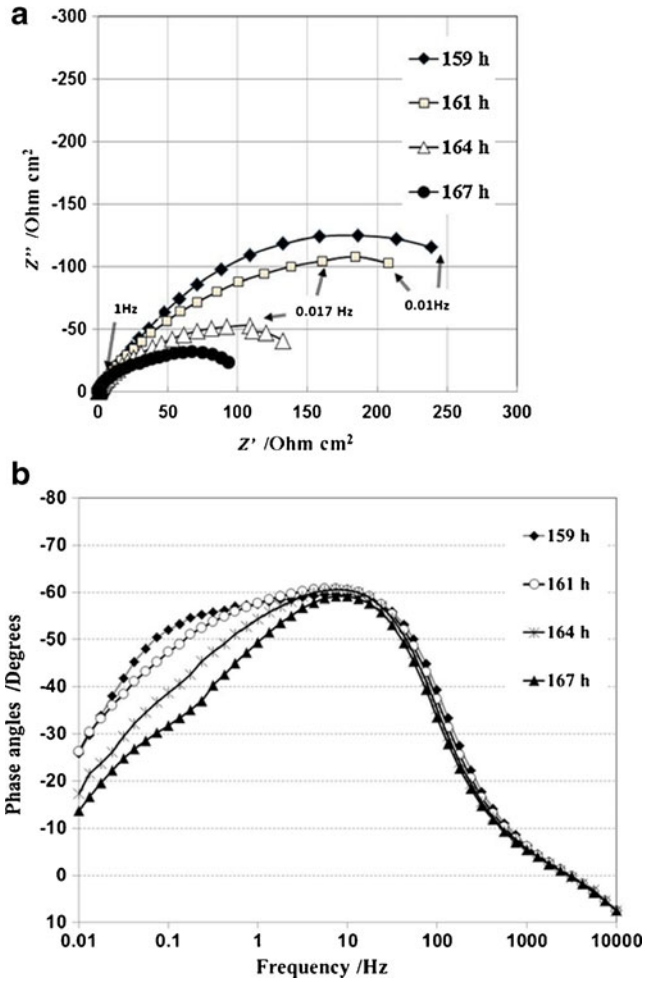

Fig. 5 EIS Nyquist plot (**b**) and phase angle plot (**b**) at different times of exposure to a 3 wt.% NaCl solution for stage 4

Z_{lw} as the lateral wall impedance of the pore. Previously, we [9] described the evolution of impedance by dynamic layer changes and assumed that the total surface area was controlled by a transport mechanism. In the present case, the charge conservation is applied to each subdivision of the loop element; the expressions integrate the scale factor by compiling all mechanisms in one network [29]. The general expressions for the charge balance for each element are defined as:

$$\frac{d^2 i_{we}}{dx^2} - \tau i_{we} + \frac{R_e}{Z} I = 0 \quad (1)$$

$$\frac{d^2 i_e}{dx^2} - \tau i_e + \frac{R_{we}}{Z} I = 0 \quad (2)$$

$$\frac{d^2 E}{dx^2} - \tau E = 0 \quad (3)$$

where R_{we} and R_e are the resistances of the steel/electrolyte interface, and of the CO_2 electrolyte solution per length respectively as represented in Fig. 6. Also, i_{we}, and i_e, are the currents in the electrode and the solution respectively.

Equations (1) to (3) were derived with the boundary conditions as in [20] of the semi-infinite cylindrical pore. The current and voltage, defined as I and E, respectively, represent the conditions at the pore mouth when $x=0$ and when $x=L$ at the base of the pore, where L is the length of the pore. By solving the simultaneous system expressions (1) to (3) with the respective boundary conditions represented in the x direction or perpendicular to the fluid, the total impedance of a cylindrical pore was calculated as:

$$Z_{pp} = \frac{R_{we} R_e L}{R_e + R_{we}} + \frac{2\zeta^{0.5} R_{we} R_e + \zeta^{0.5}\left(R_{we}{}^2 + R_e\right)\Gamma + \lambda R_e \Phi}{\zeta^{0.5}(R_{we} + R_e)\left(\zeta^{0.5}\Phi + \lambda\Gamma\right)} \quad (4)$$

where $\Phi=\cosh(\zeta^{0.5}\lambda)$; $\Gamma=\sinh(\zeta^{0.5}\lambda)$; and $\zeta = \frac{R_{we}+R_e}{Z_{lw}}, \lambda = \frac{R_{we}+R_e}{Z_b}$, Z_{lw} is the impedance of the lateral's pore wall, Z_b is the impedance of the base pore, and L is the length of the pore.

Expression (4) which was originally derived by Park and Macdonald [20] has been calculated elsewhere by several authors for different systems [17, 30]. Kramers–Kronig transforms [27] were used in this work to confirm the use of impedance during the evolution process. Three stages were identified in a previous work [9] for the electrode surface by assuming two homogenous layers. In this work, the formation of a homogeneous porous layer due to selective dissolution is assumed to be occurring at stage 1.

The porous layer formed during the activation stage is associated with the charge transfer process at the metal/electrolyte interface; the hydrogen reduction reaction takes place at the pore surface where the Fe_3C remains as the wall of the porous layer [31]. Previous studies have described the active state or charge transfer state as a hydrogen buffering process as a result of the chemistry of the solution within the pores [32]. Also, there has been a different hypothesis that has been formulated for the activation state as a consequence of a nonlinear response at the interface that is caused by the process rate being faster than the transfer function response, and also an analogy to inductance behavior in the impedance spectra that resulted from the adsorption and desorption process [33]. After selective metal dissolution, the surface modification assumes the formation of cylinder pores, where the lateral wall and the base surface influence the active reaction in stage 1.

The equivalent circuit analog representing the mechanisms in stage 1 includes a pseudocapacitor in parallel with a resistor, with the resistance acting as the charge transfer element at the base and the wall of the pore as shown in Fig. 7a. Stage 2 characterizes the mechanisms within the formed cylindric pore, and separates the influence of the base and the lateral wall from the impedance distribution owing to corrosion products formation. We assume that the

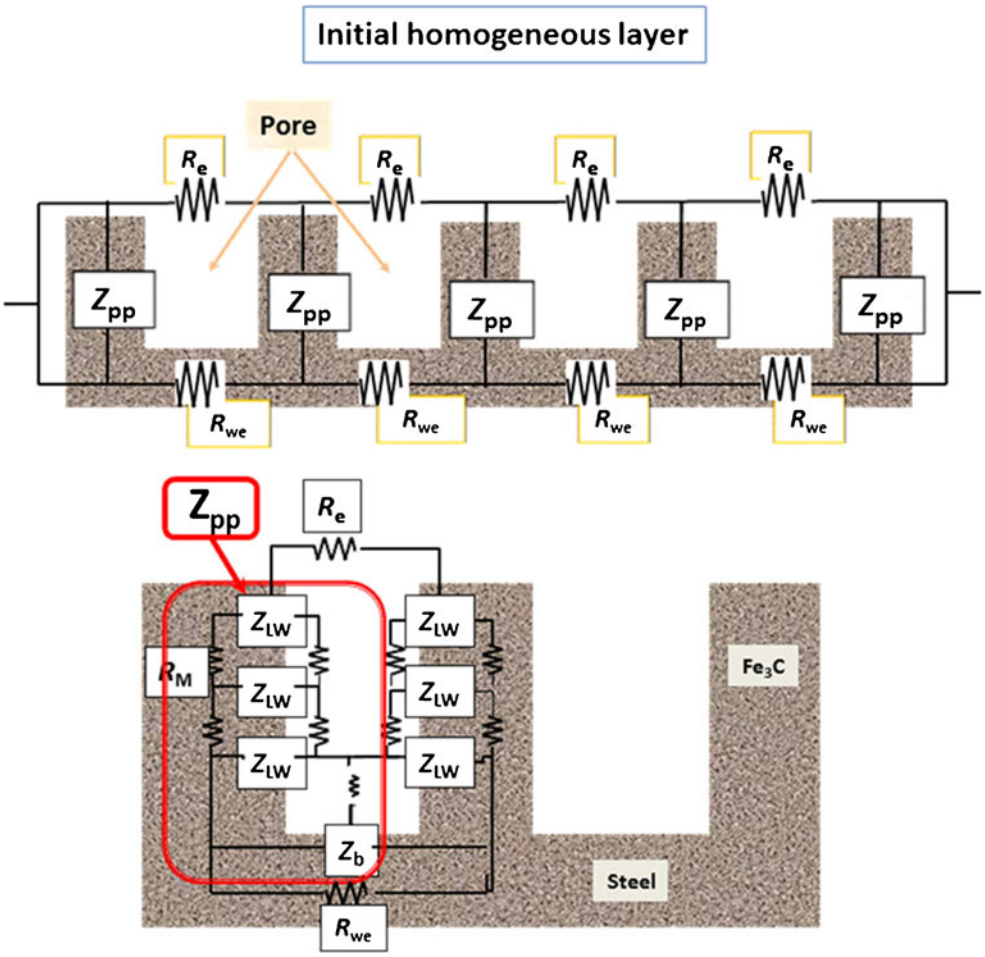

Fig. 6 Scheme of the homogeneous cylindrical pore and its components represented by Z_b as the base of the pore and Z_{lw} as the lateral wall of the pore cylinder and Z_{pp} as the impedance per pore

precipitation of the mesoporous layer of corrosion products within the pores occurs initially at the base as a result of influence of the electrolyte chemistry [6, 32]. Iron carbonate is assumed to form initially at the base of the pore. The equivalent circuit analog for Stage 2 is represented in Fig. 7b. The interfacial processes at the pore base include the charge transfer reaction and linear mass transfer in series. The pseudo-capacitance due to the corrosion mesoporous layer distribution is considered in parallel. The circuit analog describes the evolution of the precipitation of $FeCO_3$ at the base, whereas the wall is assumed to be formed by resistance in parallel with a pseudo-capacitance that describes the Fe_3C with charge transfer influence. Stage 3 includes the analogs for the pore base as two processes influenced by the corrosion product. The continuous growth of the corrosion product at the bottom part produces a pseudo-capacitance with parallel resistance at the interface of the wall surface, and the analogs for the elements of the TL used are same as stage 2. The third stage includes the precipitation and growth of the corrosion products layer at the pore base and initiation at the bottom of the surface wall of the cylindrical pores [34, 35] as displayed in Fig. 7c. Stage 4 reactivates the surface by initiating the breakdown of the corrosion product layer. The analogs representing the interface are active–passive in nature, where the highest surface exposed to the electrolyte influences the active process in this case the pore wall, and the region of the highest passive representation is the base of the pore, as shown in Fig. 7d.

Figure 8 shows a schematic representation of the evolution processes at the steel/electrolyte interface within the homogeneous and steel/corrosion products/electrolyte interface.

The TL element representing the active state was associated with the atomic hydrogen charge transfer process, and was represented with a pseudo-capacitance element in parallel to the resistance, as described in Eq. 5 and represented in the base and wall pore in Fig. 7a and wall pore in Fig. 7b, c, and d:

$$Z_{ct} = \frac{R_p}{1 + \left(R_p j\omega Q_p\right)^{\alpha_{ct}}} \tag{5}$$

where R_p=pore resistance ascribable to the charge transfer mechanism, α_{ct}=dispersion or roughness factor, and Q_p= pseudo-capacitance.

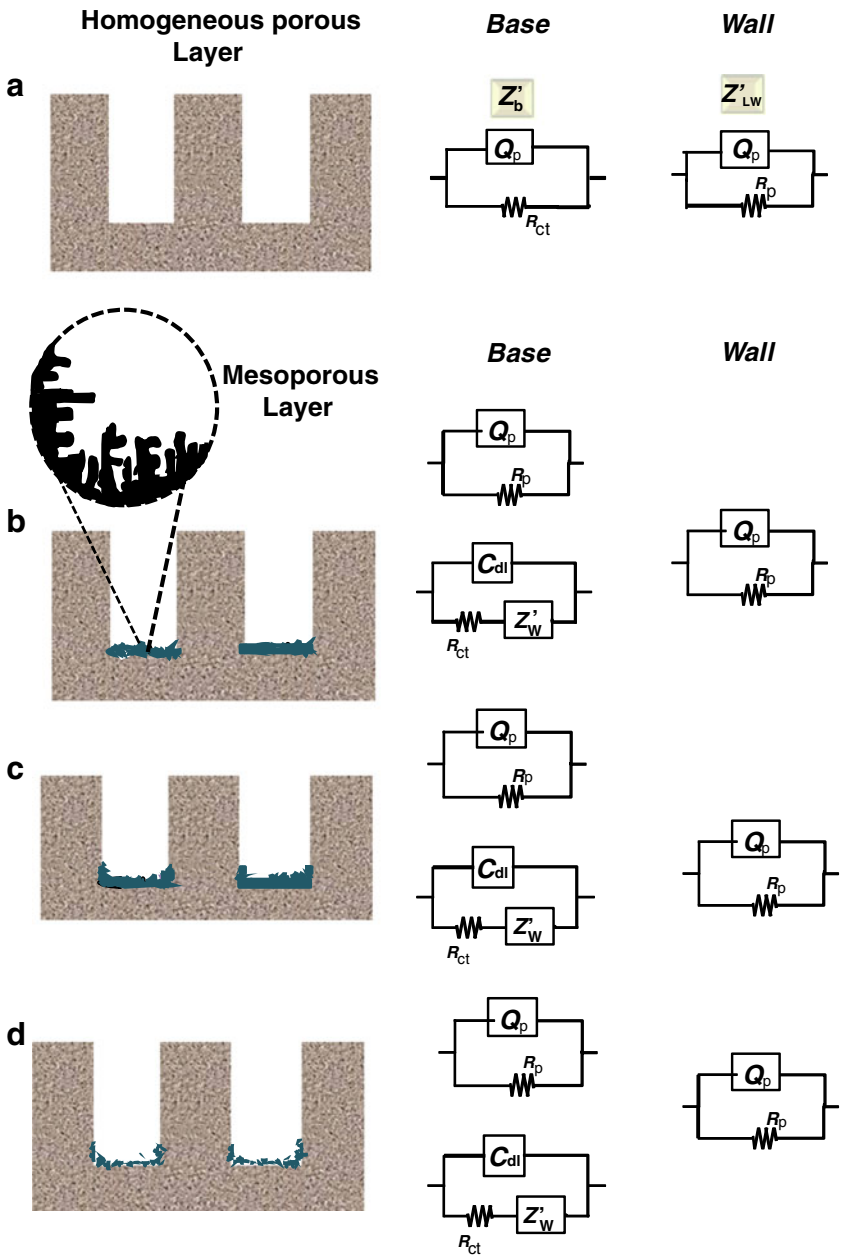

Fig. 7 Scheme of the homogeneous cylindrical pore and the mesoporous layer formed within th homogenous porous layer, the analog elements represented by Z_b as the base of the pore and Z_{lw} as the lateral wall of the pore cylinder. **a** Formation of homogeneous porous layer in stage 1, **b** formation of mesoporous layer in stage 2, **c** mesoporous layer in stage 3, **d** mesoporous breakdown in stage 4

Stages 2, 3, and 4 includes locations for the charge transfer process caused by the hydrogen reaction, and the mass transfer associated with the diffusion of HCO_3 ions both happening at the interface due to active–passive process at the interface of the base/wall pore with electrolyte. Equation 6 describes the impedance of one element of the transmission line for the active–passive process:

$$Z_{tm} = \frac{R_{ct} + Z_w}{1 + (R_{ct} + Z_w)(j\omega C_{dl})^{\alpha_{tm}}} \tag{6}$$

where R_{ct}=charge transfer resistance attributable to the H^+ charge transfer, Z_w is the Warburg impedance caused by the bicarbonate/iron diffusion through the $FeCO_3$ porous media, C_{dl}=double layer capacitance, and α_{tm}=constant associated to porous $FeCO_3$ layer roughness and impedance dispersion [17, 19].

Stages 2, 3, and 4 characterize the influence of the mesoporous $FeCO_3$ layer formation at the interface of the steel pore with electrolyte. Equation 7 describes the influence of each stage either passive or active as previously reported by Castaneda [36] in the impedance of

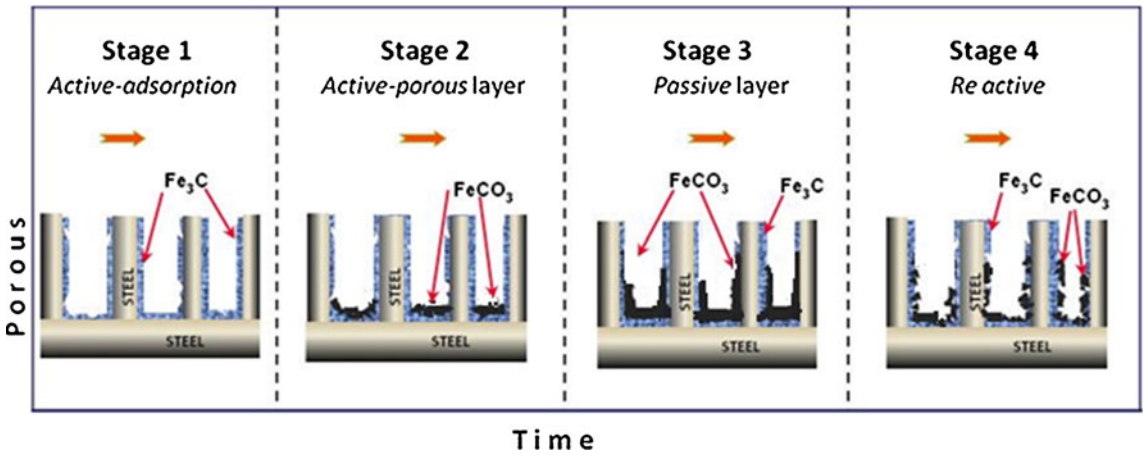

Fig. 8 Schematic representation of the evolution processes at the steel/corrosion products/electrolyte interface in the homogeneous cylindrical pore

one element of the transmission line in this case related to the $FeCO_3$ mesoporous layer or mixture active–passive process:

$$Z_{ap} = \frac{Z_{ct}Z_{tm}}{Z_{tm}\phi + Z_{ct}(1-\phi)} \tag{7}$$

where Z_{ap} is the influence of the active and passive state at Φ ratio, where Φ=1 is charge transfer influence and Φ=0 is mass transfer mechanism influence. Z_{ct}= impedance for active state influence, Z_{tm}=impedance for mass transfer influence.

Geometry factor is considered for the homogeneous porous layer formed initially at stage 1. A cylindrical shape of the pores is assumed, while the area of the base and the wall are calculated respectively as πr^2 and $2\pi rl$. The area coverage of the mesoporous corrosion product at the interface for the base is represented by θ_b and for the wall, θ_w. Therefore the impedance of the wall and the pore base due to the interface substrate/corrosion products defined in expression 4 is:

$$Z_{lw} = Z'_{lw} n^{0.5} (2\pi^{0.5}(1-\theta_w)^{0.5} A^{0.5} \tag{8}$$

$$Z_b = Z'_b n/(1-\theta b)A \tag{9}$$

where n is the number of pores in homogeneous layer, A is the total surface area, Z'_{lw} and Z'_b are the specific impedances for the wall and pore base respectively which can be represented by either expressions 5, 6, or 7. This latter depends on the stage governing the interface. Figure 7 represents the specific impedances for each stage. Stage 1 considers Z'_{lw} and Z'_b being equal to the expression 5 for Z_{ct}. Stages 2, 3, and 4 considers Z'_{lw} being equal to expression 5 while Z'_b equals to expression 7.

Consequently, the total impedance at the interface composed of n number of pores is represented with the following Eq. (10):

$$Z_T = \left(\frac{Z_{pp}}{n}\right) = \frac{1}{n}\left(\frac{R_{we}R_eL}{R_{we}+R_e} + \frac{2\zeta^{0.5}R_{we}R_e + \zeta^{0.5}\left(R_{we}^2+R_e^2\right)\Gamma + \lambda R_e^2\Phi}{\zeta^{0.5}\left(R_{we}^2+R_e^2\right)\left(\zeta^{0.5}\Phi+\lambda\Gamma\right)}\right) \tag{10}$$

Figure 8 illustrates the $FeCO_3$ evolution within the pore's homogeneous layer. The stabilization and evolution of $FeCO_3$ is the major influencer for the interfacial process. Nesic has found the $FeCO_3$ layer was formed after more than 60 h [28, 37]. It was assumed in this work that the corrosion products layer has been formed between 65 and 155 h. The addition of sulfuric acid resulted in the breakdown of the passive layer formed in previous stages as a consequence of the chemical composition within the pores in the electrolyte.

During stage 4, the corrosion product porous layer experienced breaks and defects in the mesoporous layer. Castaneda et al. showed that TL characterize the iron sulfur corrosion products [17], and the corrosion layer evolved according to the chemistry within the pore as a result of different pH conditions affecting the wall and the base of the pore. Macdonald et al. [38] characterized nickel secondary battery performance and pore evolution by assuming two different corrosion products at the interface. The heterogeneous layer was originated by the products formed as a consequence of different charge and discharge cycles. During this work, a steady-state condition is assumed to exist for each stage, and the impedance distribution of the pore was modified owing to the corrosion product that grew at different locations.

Quantification of parameters at the interface by TL modeling

Evolution of the porous interface is quantified by TL modeling per stage. A computer program was developed by using Matlab software and the expressions obtained previously. Table 1 summarizes the evolution of the parameters used for the fitting process with time. Eleven parameters were considered for the fitting-analysis process for stages 1 and 2. The parameters related to the characteristics of the elements associated to the pore are: R_p=charge transfer resistance for active interface, R_{ct}=charge transfer resistance for the active–passive interface, Q_p=double layer pseudo-capacitance for active mechanism, C_{dl}=porous pseudo-capacitance for the active–passive mechanism, n=number of pores, σ=Warburg coefficient, θ_b=pore base cover, θ_b=pore wall cover, α_{ct}=roughness parameter for active interface, α_{ct}=roughness parameter for passive interface and Φ=a dimensional parameter for active–passive state mechanism influence. The independent parameters describe the evolution of the interface representing each stage. Stage 1, which is the active state, is influenced by the charge transfer process within the pore characterizing the interface at the wall and pore base. The magnitude associated with the wall and the pore base is charge transfer resistance for the wall surface, R_p and the pore base R_{ct}, respectively. The lateral pore wall surface area is assumed to be constant during the four stages. During stage 1, the impedance evolution is influenced by the base pore surface, and the R_{ct} magnitude decreases due to the reaction sites available for the adsorption/charge transfer reaction. The feasibility for forming $FeCO_3$ has been characterized by the SS parameter [6, 28, 39]. The initial conditions magnitude illustrates for SS_0=12 in previous work [9], during stage 1 the SS increases to a magnitude of 20.

Table 1 displays the charge transfer resistance fitting magnitudes at different times for stage 1. The active or stage 1 and active–passive or stage transition process is identified by resistance and capacitance trends in magnitudes. These parameters R_p, R_{ct}, Q_p, and C_{dl} represents the evolution of the mechanisms at two different locations within the pore, the wall and the pore base. Our previous work [9] showed same order of magnitude for pseudo-capacitance using equivalent circuit analysis with the capacitance estimated from TL of 1×10^{-4} μF cm^2 s n^{-1} by the pore base and different magnitudes founded for the wall surface of 1×10^{-6} μF cm^2 s n^{-1}. The transition active–passive process identifies the formation of a $FeCO_3$ layer at the pore base; the cylindrical geometry of the pore influences the Fe^{2+} and CO_3^{-2} concentration gradient and profile within the pore. The stage 2 process starts at 25 h of exposure. Pore base impedance is influenced by the mass transport process. The C_{dl} [40, 41] evolution represents the coverage of the corrosion product at the pore base, the pseudo-capacitance magnitude is influenced by the thickness and conductivity of the corrosion product, α_{tm} parameter resolves the roughness of the $FeCO_3$ porous layer also the mass transport evolution is reflected by the diffusion coefficient within the pore by estimating a magnitude of 1.3×10^{-10} cm^2 s^{-1}. Diffusion coefficient for HCO_3^- has been reported for aqueous environments at similar conditions of aqueous solutions [42] as 2.83×10^{-10} cm^2 s^{-1}.

Lateral wall in stage 2 was characterized with charge transfer, pseudo-capacitance, and no implications of mass transfer element and $FeCO_3$ formation. The base pore includes the increment of the charge transfer resistance, R_{ct} and pseudo-capacitance, C_{dl} with time, the first influenced by the availability sites to charge transfer at the interface, and the second caused by the mesoporous layer thickness and electrical properties evolution. The diffusion of ionic species within the layer is characterized by the σ (Warburg coefficient) magnitude; this latter appears during the transition from stage 1 to stage 2. The layer grows from the base to the pore mouth through the bottom of lateral walls as illustrated in Fig. 7b.

Table 2 displays the fitting parameters for stages 3 and 4. The parameters Q_p, R_p represent the evolution of the interface at the lateral wall and R_{ct}, C_{dl} characterize the pore base. While stage 3 is characterized by the formation and

Table 1 Values corresponding to different elements after a fitting with TL was applied to impedance evolution during stage 1and 2 for steel surface exposed to a 3 wt% NaCl, CO_2 partial pressure of 5.4×10^4 Pa at 80°C

Time (h)	Pores (#)	Pore wall surface			Pore base					SS ($FeCO_3$)
		From expression 5			From expression 7					
		Q_p μF cm^2 s n^{-1}	R_p (Ω cm^2)	α_{ct}	C_{dl} μF cm^2 s n^{-1}	R_{ct} (Ω cm^2)	α_{tm}	Φ	σ Coeff	
9	1000	1×10^{-6}	15	0.98	1×10^{-4}	268	0.90	1	–	14
12	1000	1×10^{-6}	15	0.98	1×10^{-4}	260	0.90	1	–	16
18	1000	1×10^{-6}	15	0.98	1×10^{-4}	255	0.90	1	–	18
25	1000	3×10^{-6}	25	0.97	6×10^{-4}	236	0.90	0.84	65	21
45	1140	3×10^{-6}	28	0.97	6.5×10^{-4}	238	0.89	0.84	70	22
65	1140	3×10^{-6}	35	0.97	6.8×10^{-4}	286	0.89	0.84	100	17
75	1140	3×10^{-6}	40	0.97	6.9×10^{-4}	326	0.87	0.84	130	15

grow of mesoporous of $FeCO_3$ layer, the R_{ct} magnitudes increase with time and are in the same order of magnitude as estimated previously [9]. The corrosion products layer is assumed to form and grow with time as illustrated in Fig. 7c and the charge transfer resistance magnitude at the base is higher than the wall surface because of the lesser number of sites available for the mechanism. The number of pores for the homogenous inner layer remains constant for the calculations by assuming the maximum number is reached during stage 2. Selective dissolution occurs at ferrite sites where homogeneous porous density is assumed to be formed at 3 h. Stage 2 is dominated by the activation at the pore walls and active-mass transfer at the pore base, the number of homogeneous pores is defined at this stage 2 to be 1140. Stage 3, the passive state, started at 85 h and finished at 155 h when the evolution of mesoporous layer within the homogeneous porous shows active and mass transfer indicative parameters. The contribution of mass transfer process at the pore base, defined as Φ, decreases to a magnitude of 0.14. The influence at the base of the pore is higher for mass transfer, the pseudo-capacitance decrease slightly and the resistance increase. The evolution at the base considers the grow of the mesoporous layer, the pseudo-capacitance is lower than previous estimations as a result of formation at the pore base and the denser mesoporous layer at the confined area, the resistance is higher in magnitude as previously reported as a result of the less sites available for charge exchange reaction; the wall surface pseudo-capacitance and resistance remained constant with time as displayed in Table 2.

Farelas et al. [9] assumed a gradual cover of the pore surface by iron carbonate starting at stage 3. TL modeling helped to understand the nature of the growing mesoporous layer by representing the precipitation initiation and evolution at the pore base during stage 2 and evolution at the base and bottom of the wall during stage 3. The influence of the mechanism existed at the interface steel/pore base layer was characterized by parameter Φ, the active-mass transfer mechanism parameter. The passive state at the pore base predominated with time during stage 3. The mass transport factor σ used for pore base displays increasing magnitude with time; the C_{dl} parameter evolves with time where the coverage of the base is proportional to its magnitude [16, 19]. Devos et al. illustrate the evolution of the scaling environment with time by measuring C_{dl} with imaging coverage of the entire surface [43]. They also quantified the evolution of an electrode blocked by the corrosion product with a dimensional parameter, S for coverage. Castaneda et al. [17] estimated the coverage of corrosion products by measuring the capacitance magnitude in the iron sulfur pore surface by separating the base and the wall pore locations and using TL modeling. Stages 2 and 3 show the R_p, Q_p, and α magnitude evolution with time, as the mesoporous products/homogeneous pore walls gradually reach changes in properties at 85 h. The control mechanism at the interface of the wall pore is dominated by the charge transfer reaction. R_p and Q_p magnitudes increase with time, the range of the magnitudes estimated can be compared with the previous work [9] where the R_{ct}, R_p magnitudes range from 17 to 47 Ω cm^2 while Q_p and C_{dl} were from 183 to 3100 μF cm^2 s n^{-1} in active and active–passive transition stages respectively. Farelas et al. [9] assumed different layers of different thickness between the electrolyte/electrode interfaces. Equivalent circuits described the evolution in each layer and in this work the subdivision of the interface in two layers, one inner porous homogeneous with separation of base and wall and the outer mesoporous layer could describe the influence of the mechanisms in each

Table 2 Values corresponding to different elements after a fitting with TL was applied to impedance evolution during stages 3and 4 for steel surface exposed to a 3 wt% NaCl, CO_2 partial pressure of 5.4×10^4 Pa at 80°C

Time (h)	Pores (#)	Pore wall surface			Pore base					SS ($FeCO_3$)
		From expression 5			From expression 7					
		Q_p μF cm^2 s n^{-1}	R_p (Ω cm^2)	α_{ct}	C_{dl} μF cm^2 s n^{-1}	R_{ct} (Ω cm^2)	α_{tm}	Φ	σ Coeff	
85	1140	3×10^{-6}	42	0.97	1.3×10^{-4}	570	0.83	0.14	7500	13
95	1140	3×10^{-6}	45	0.97	1.4×10^{-4}	700	0.83	0.14	8900	12
105	1140	3×10^{-6}	47	0.96	1.4×10^{-4}	960	0.83	0.14	6900	10
115	1140	3×10^{-6}	46	0.96	1.2×10^{-4}	1690	0.80	0.14	4300	8
135	1140	3×10^{-6}	49	0.97	9.9×10^{-5}	2030	0.78	0.14	2300	8
155	1140	3.3×10^{-6}	49	0.96	9.9×10^{-5}	2300	0.77	0.14	2100	7
159	1140	1×10^{-6}	10	0.96	1×10^{-3}	770	0.86	0.09	14000	2
161	1140	1×10^{-6}	10	0.99	1×10^{-3}	730	0.88	0.1	6500	1
164	1140	1×10^{-6}	10	0.99	1×10^{-3}	230	0.91	0.1	3300	0.3

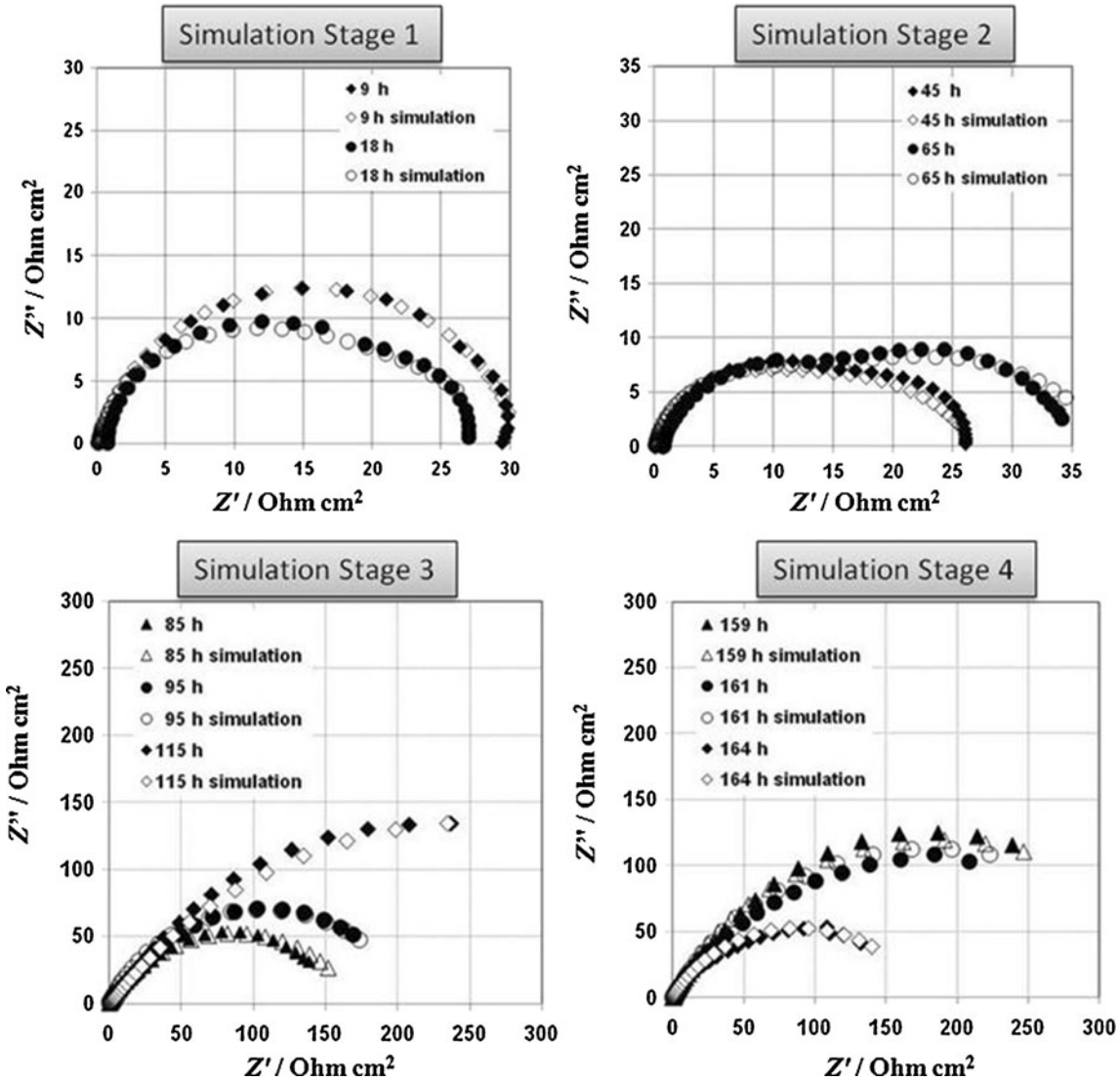

Fig. 9 Comparison of LPR and TLM corrosion rates vs. time for a carbon steel 1018 electrode at different stages during the CO_2 corrosion process

interface formed. During stages 2 and 3, the pore walls are partially covered by the $FeCO_3$ mesoporous layer at the bottom, the precipitation at the base consumes the Fe^{2+} ions and depletes the concentration.

Linear polarization resistance has been used as the prime electrochemical method to estimate the corrosion rate when steel is exposed to a CO_2 environment for different lengths of time [36, 44]. The physical parameters of the passive layer evolve, and consequently from the kinetics of layer growth/formation, the steady-state nature of the interface has permitted the use of low polarization techniques such as LPR and EIS, which are small-amplitude techniques that are used to monitor change of the interface. One advantage of DC-based technique, such as LPR is the quick response for estimation of the overall rate, whereas techniques based on AC give insights to the mechanisms and the separation of the elements at the interface by the wide frequency range describing the interface.

The number of pores, characteristics of the pore, and the elements fitted for the four stages represent the evolution of the active, active-mass transfer and reactivation process at the interface. Tables 1 and 2 shows the evolution within a pore separated in two locations, base and lateral wall charge transfer and mass transfer processes as they relate to the dissolution process. Castaneda et al. [36] estimated the dissolution process by linking alternate current and the TL for a high resistivity electrolyte with charge and mass transfer mechanisms for each element forming the TL [17]. Corrosion rate was estimated for each stage by using R_{ct}, Z_w parameters and as described previously by Castaneda [36]. Tables 1 and 2

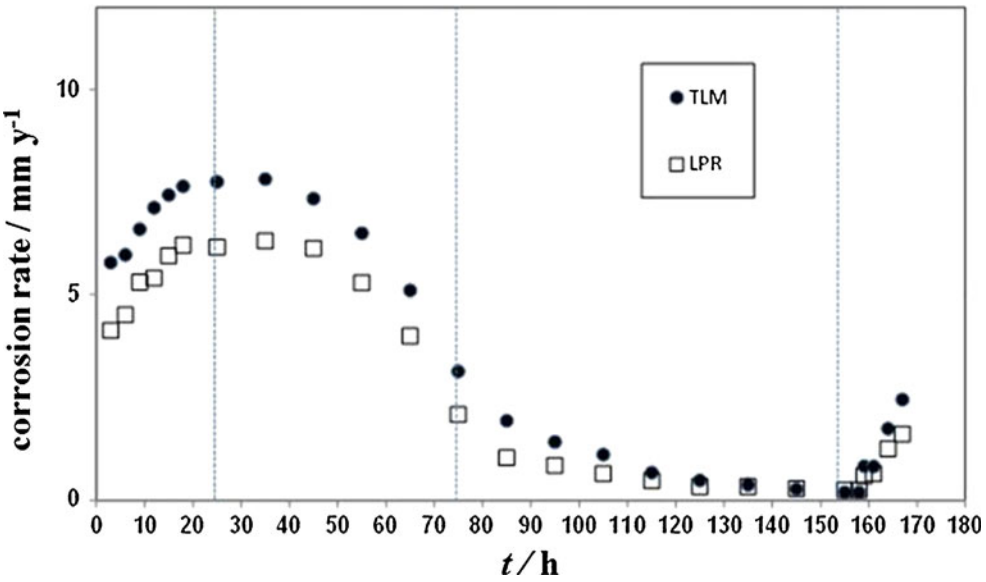

Fig. 10 Comparison of experimental impedance and TL simulation diagrams for the four stages of the evolution processes

represent the evolution of the elements at the interface within the pore, such as R_{ct}, R_p, Q_p, C_{dl}, σ, and α for each stage. Several authors have demonstrated the stability of the corrosion products layer [3, 4, 7, 9, 34, 35] attributable to $FeCO_3$ precipitation and formation. The separation of the elements of the pore showed the controlled process to be charge transfer and mass transfer at the base and following certain critical time. The influence of the pore base interface leads to the stabilization of the charge transfer and mass transfer mechanisms. The corrosion rate at stage 3 decreases, while the charge transfer at the wall and pore base increases. Surface area for active–passive state is a function of precipitation and formation of corrosion products, such as $FeCO_3$.

Stage 3 is modified by adding H_2SO_4 solution to the electrolyte. In doing so, SS magnitude decreases and the pH of the electrolyte changes to a magnitude approximately of 5. The chemistry within the pore is modified, and pseudo-capacitance magnitudes indicate the coverage modification was caused by the breakdown of the mesoporous layer and the leak current with the charge transfer decreasing the magnitude and originating higher dissolution rate. The activation of the interface is considered at this stage at both locations within the pores. Table 2 displays the pore base magnitudes associated with the evolution at the interface, breakdown of the layer created sites for exchange reaction to magnitudes equivalent to stage 1. R_{ct} reached 230 Ω cm^2 in stage 4, same parameter was 236 Ω cm^2 at the end of stage 1. Pseudo-capacitance was higher in magnitude than stage 1 following the breakdown or stage 4. This latter could be as a consequence of the mesoporous evolution at the homogeneous porous layer/electrolyte interface as illustrated in Fig. 7d, the surface increase the sites where the current drain. Figure 9 shows the fitting magnitudes vs. the experimental parameters for different times in each one of the four stages.

The fitting process for each stage includes a minimum square error method. The expression 10 was used to fit the data displayed in Fig. 9 and validate the confidence by using minimum squares MSQ in Eq. (11):

$$\mathrm{MSQ} = \sum \frac{\left[\left(Z^{\mathrm{real}}_{\mathrm{T,\,Exp}} - Z^{\mathrm{real}}_{\mathrm{T}}\right)^2 + \left(Z^{\mathrm{imaginary}}_{\mathrm{T,\,Exp}} - Z^{\mathrm{imaginary}}_{\mathrm{T}}\right)^2\right]}{\left[Z^{\mathrm{real}}_{\mathrm{T,\,Exp}} + Z^{\mathrm{imaginary}}_{\mathrm{T,\,Exp}}\right]} \tag{11}$$

where $Z_{T,Exp}$ is imaginary and real impedance of the experimental data to fit, Z_T is the theoretical impedance. The algorithm developed includes an error percentage of 5% maximum as a stop criterion for each frequency included. Figure 10 shows the corrosion rate evolution, with time calculated from DC and AC measurements. Qualitatively, the magnitudes are similar for both approaches; detailed analysis with TL modeling reveals the evolution of the mechanism in early stages (1 and 2) produce higher dissolution rates magnitudes. Surface area in TLM includes the characteristics of the pore, such as the number of pores, the cover factor and the elements describing the interface stage before and after the layer formation and after breakdown. Charge transfer resistance in the four stages represents the active sites available from the dissolution process, whereas the C_{dl} magnitude represents the physical nature of the aqueous-film interface and quantifies the passive sites. Figure 10 indicates the corrosion rate evolution per stage. Differences in corrosion rate for AC and DC approaches show the implications of both techniques; the highest magnitude for corrosion rates during stages 1 and 2 for AC-TLM represents the detailed modification and influence of surface available for the active sites. Higher magnitudes for impedance and resistance at the pore base reveal the influence of this interface in the corrosion rate. Selective dissolution and active sites originated

the pores and the influence of the charge transfer mechanism. Stages 1, 2, and 4 include the highest influence as a result of the active surface area mechanism within the pore. During stage 3, the corrosion rate is quantitatively similar in both techniques as a consequence of the mesoporous formation of the $FeCO_3$ layer; the active/passive area ratio is similar during this stage. Farelas [26] reported different SEM images of X65 steel coupons exposed in flow channel cell at same electrolyte conditions as the present work, the $FeCO_3$ layer formed at the base of the pore did not precipitate at the pore mouth and the middle-upper part of the wall surface of the pores during the exposure time equivalent to our stage 3.

Conclusions

TL modeling characterized and quantified the evolution of the mechanisms through the parameters associated with the elements of the network at the interface electrode/electrolyte.

The separation of the base and the wall of the initial homogeneous porous layer having a cylindrical geometry describe the precipitation and the formation of the mesoporous $FeCO_3$ layer. The four stages identified the dissolution mechanisms attributable to the modification of the pH, transport, and interfacial mechanisms. The elements defined at the pores describe qualitatively the evolution at each location of the pore.

The precipitation of $FeCO_3$ porous layer was initiated and grows at the base and the middle-upper part of the wall remained active as a result of the chemistry, composition, and geometry of the wall surface within the pore. This latter marked the influence of the overall mechanism of the pore base over the surface wall.

TLM by means of impedance measurements could estimate the dissolution rate and elucidate the mechanisms in real time of the steel/CO_2 electrolyte system.

Acknowledgments Monica Galicia acknowledges F. Farelas for the experimental data that was used in this research while he developed part of his Ph.D. at the Institute for Corrosion and Multiphase Technology of Ohio University.

References

1. Zheng D, Che D, Liu Y (2008) Experimental investigation on gas–liquid two-phase slug flow enhanced carbon dioxide corrosion in vertical upward pipeline. Corros Sci 50:3005–3020
2. López DA, Pérez T, Simison SN (2003) The influence of microstructure and chemical composition of carbon and low alloy steels in CO_2 corrosion. A state-of-the-art appraisal. Mater Des 24:561–575
3. Foss M, Gulbrandsen E, Sjöblom J (2009) Effect of corrosion inhibitors and oil on carbon dioxide corrosion and wetting of carbon steel with ferrous carbonate deposits. Corrosion 65:3–14
4. Louafi Y, Ladjouzi MA, Taibi K (2010) Dissolved carbon dioxide effect on the behavior of carbon steel in a simulated solution at different temperatures and immersion times. J Solid State Electrochem 14:1499–1508
5. Guo XP, Tomoe Y (1999) The effect of corrosion product layer on the anodic and cathodic reactions of carbon steel in CO_2 saturated MDEA solutions at 100°C. Corros Sci 41:1391–1402
6. Zhang GA, Cheng YF (2009) Corrosion of X-65 steel in CO_2 saturated oil field formation water in the absence and presence of acetic acid. Corros Sci 51:1589–1595
7. Nesic S (2007) Key issues related to modeling of internal corrosion of oil and gas pipeline—a review. Corros Sci 49:4308–4338
8. Nesic S, Nordsveen M, Nyborg R, Stangeland A (2003) A mechanistic model for carbon dioxide corrosion of mild steel in the presence of protective iron carbonate films-part 2: a numerical experiment. Corrosion 59:489–497
9. Farelas F, Galicia M, Brown B, Nesic S, Castaneda H (2010) Evolution of dissolution processes at the interface of carbon steel corroding in a CO_2 environment studied by EIS. Corros Sci 52:509–517
10. Castaneda H, Benetton XD (2008) SRB-biofilm influence in active corrosion sites formed at the steel-electrolyte interface when exposed to artificial seawater conditions. Corros Sci 50:1169–1183
11. Castaneda H, Tan B, Saunders J (2010) Electrochemical characterization of the LiCoO2/acetylene carbon ratios for porous electrodes in alkaline lithium aqueous solutions by electrochemical impedance spectroscopy. Electrochim Acta 55:4137–4143
12. Yu B, Jin Q, Ding D, Li B, Shi AC (2008) Confinement induced morphologies of cylinder-forming asymmetric diblock copolymers. Macromolecules 41:4042–4054
13. Latz A, Zausch J (2011) Thermodynamic consistent transport theory of Li-ion batteries. J Power Sources 196:3296–3302
14. Shayegani M, Afshar A, Ghorbani M, Rahmaniyan M (2008) Mild steel carbon dioxide corrosion modeling in aqueous solutions. Corros Eng Sci Technol 43:290–296
15. Elliott JM, Owen JR (2000) Electrochemical impedance characterization of nanostructured (mesoporous) platinum film. Chem Phys 2:5653–5659
16. Song H, Jung Y, Lee K, Le Dao H (1999) Electrochemical impedance spectroscopy of porous electrodes: the effect of pore size distribution. Electrochim Acta 44:3513–3519
17. Castaneda H, Sosa E, Espinosa-Medina MA (2009) Film properties and stability influence on impedance distribution during the dissolution process of low-carbon steel exposed to modified alkaline sour environment. Corros Sci 51:799–806
18. De Levie R (1963) On porous electrodes in electrolyte solutions. Electrochim Acta 8:751–780
19. De Levie R (1967) Electrochemical response of porous and rough electrodes. Adv Electroch El Eng 6:329–397
20. Park JR, Macdonald DD (1983) Impedance studies of the growth of porous magnetite films on carbon steel in high temperature aqueous systems. Corros Sci 23:295–315
21. De Levie R (1965) The influence of surface roughness of solid electrodes on electrochemical measurements. Electrochim Acta 10:113–130
22. Pell WG, Conway BE (2001) Voltammetry at a de Levi brush electrode as a model for electrochemical supercapacitor behaviour. J Electroanal Chem 500:121–133
23. Candy JP, Fouilloux P, Keddam M, Takenouti H (1982) The pore texture of Raney-nickel determined by impedance measurements. Electrochim Acta 27:1585–1593
24. Meyers JP, Doyle M, Darling RM, Newman J (2000) The impedance response of a porous electrode composed of intercalation particles. J Electrochem Soc 147:2930–2940

25. Paasch G (2004) Transport in doped conjugated polymers with polarons and bipolarons forming complexes with counter ions. Solid State Ionics 169:87–94
26. Farelas F (2010) Electrochemical study of the evolution of dissolution and inhibition processes at the interface of 1018 and X65 carbon steels exposed to CO_2 environment using a linear flow cell and rotating cylinder electrode. Ph.D. dissertation, Instituto Mexicano del Petroleo
27. Macdonald DD, Urquidi-Macdonald M (1990) Kramers–Kronig transformation of constant phase impedances. J Electrochem Soc 137:515–518
28. Sun W, Nesic S (2008) Kinetics of corrosion layer formation: part 1—iron carbonate layers in carbon dioxide corrosion. Corrosion 64:334–346
29. Franco AA, Schott P, Jallut C, Maschke B (2006) A dynamic mechanistic model of an electrochemical interface. J Electrochem Soc 153:A1053–A1061
30. Wu S, Orazem ME, Tribollet B, Vivier V (2009) Impedance of a disk electrode with reactions involving an adsorbed intermediate: experimental and simulation analysis. J Electrochem Soc 156: C214–C221
31. Hinotani S, Ohmori Y, Terasaki F (1985) Effects of Fe_3C and Mo_2C precipitation on hydrogen diffusivity and hydrogen embrittlement in iron alloys. Mater Sci Eng 76:57–69
32. Remita E, Tribollet B, Sutter E, Vivier E, Ropital F, Kittel J (2008) Hydrogen evolution in aqueous solution containing dissolved CO_2: quantitative contribution of the buffering effect. Corros Sci 50:1433–1440
33. Li P, Tan TC, Lee JY (1996) Impedance spectra of the anodic dissolution of mild steel in sulfuric acid. Corros Sci 38:1935–1955
34. Heuer JK, Stubbins JF (1999) An XPS characterization of $FeCO_3$ films from CO_2 corrosion. Corros Sci 41:1231–1243
35. Mora-Mendoza JL, Turgoose S (2002) Fe_3C influence on the corrosion rate of mild steel in aqueous CO_2 systems under turbulent flow conditions. Corros Sci 44:1223–1246
36. Castaneda H, Urquidi-Macdonald M (2004) Detecting external failure and corrosion in coated, buried pipelines: transmission line model and experimental verification. Corrosion 60:538–547
37. Nesic S, Lunde L (1994) Carbon dioxide corrosion of carbon steel in two-phase flow. Corrosion 50:717–727
38. McDonald DD, Pound BG, Lenhart SJ (1990) The application of electrochemical impedance spectroscopy for characterizing the degradation of $Ni(OH)_2$/NiOOH electrodes. J Power Sources 29:477–502
39. Nesic S, Sun W (2010) Corrosion in acid gas solutions. In: Richardson TJA (ed) Shreir's Corrosion, vol 2. Elsevier Science Direct, pp 1270–1298
40. Rout TK (2007) Electrochemical impedance spectroscopy study on multi-layered coated steel sheets. Corros Sci 49:794–817
41. Chen HY, Jepson WP (1999) EIS measurement for corrosion monitoring under multiphase flow conditions. Electrochim Acta 44:4453–4464
42. Li YH, Gregory S (1974) Diffusions of ions in seawater and in deep sea sediments. Geochim Cosmochim Acta 38:703–714
43. Devos O, Gabrielli C, Tribollet B (2006) Simultaneous EIS and in situ microscope observation on a partially blocked electrode application to scale electrodeposition. Electrochim Acta 51:1413–1422
44. Videm K, Dugstad A (1989) Corrosion of carbon steel in an aqueous carbon dioxide environment, part 1: solution effects. Mater Perform 28:63–67